



# A spectral method solution to crystal elasto-viscoplasticity at finite strains

P. Eisenlohr<sup>a,\*</sup>, M. Diehl<sup>a</sup>, R.A. Lebensohn<sup>b</sup>, F. Roters<sup>a</sup>

<sup>a</sup> Max-Planck-Institut für Eisenforschung, Max-Planck-Straße 1, 40237 Düsseldorf, Germany

<sup>b</sup> Materials Science and Technology Division, Los Alamos National Laboratory, Los Alamos, NM 87545, USA

## ARTICLE INFO

### Article history:

Received 3 June 2012

Received in final revised form 25 August 2012

Available online 3 October 2012

### Keywords:

- A. Microstructures
- B. Crystal plasticity
- C. Numerical algorithms
- C. Finite elements
- C. High-resolution periodic volume element

## ABSTRACT

A significant improvement over existing models for the prediction of the macromechanical response of structural materials can be achieved by means of a more refined treatment of the underlying micromechanics. For this, achieving the highest possible spatial resolution is advantageous, in order to capture the intricate details of complex microstructures. Spectral methods, as an efficient alternative to the widely used finite element method (FEM), have been established during the last decade and their applicability to the case of polycrystalline materials has already been demonstrated. However, until now, the existing implementations were limited to infinitesimal strain and phenomenological crystal elasto-viscoplasticity. This work presents the extension of the existing spectral formulation for polycrystals to the case of finite strains, not limited to a particular constitutive law, by considering a general material model implementation. By interfacing the exact same material model to both, the new spectral implementation as well as a FEM-based solver, a direct comparison of both numerical strategies is possible. Carrying out this comparison, and using a phenomenological constitutive law as example, we demonstrate that the spectral method solution converges much faster with mesh/grid resolution, fulfills stress equilibrium and strain compatibility much better, and is able to solve the micromechanical problem for, e.g., a  $256^3$  grid in comparable times as required by a  $64^3$  mesh of linear finite elements.

© 2012 Elsevier Ltd. All rights reserved.

## 1. Introduction

The development of increasingly complex tools for knowledge-based design of structural materials with improved properties is a trend observed in the materials science and solid mechanics communities. The three essential requirements for such tools are the proper descriptions of (i) the physical mechanisms governing plastic deformation and evolution of microstructure, (ii) the mechanical behavior including fracture initiation at the microstructural scale, and (iii) the homogenized deformation and fracture resistance. While the development of physically appropriate models of the underlying (deformation) mechanisms is a formidable but essentially separate problem, one feasible solution to the latter two challenges is given by the use of full-field numerical simulations of volume elements that represent the microstructures in question. In order to perform such simulations, two numerical strategies are predominantly employed. In the field of crystal plasticity, a large number of investigations are based on finite element (FE) analysis (Zienkiewicz, 1967) of polycrystalline volume elements that are meshed either shape-conforming to grain boundaries or by means of regular grids, see, for instance (Cailletaud et al., 2003; Mika and Dawson, 1999; Venkataramani et al., 2008; Delannay et al., 2009; Kim et al., 2010; Clayton and McDowell, 2003; Kraska et al., 2009; Rossiter et al., 2011). An alternative to the finite element method (FEM) for solving the system of partial differential equations resulting from compatibility and static equilibrium has been introduced by Moulinec and

\* Corresponding author. Tel.: +49 211 6792 983; fax: +49 211 6792 333.

E-mail address: [p.eisenlohr@mpie.de](mailto:p.eisenlohr@mpie.de) (P. Eisenlohr).

Suquet (1994, 1998) in the context of computational homogenization. This spectral method operates in FOURIER space and is very efficient compared to FEM due to the repetitive use of a fast FOURIER transforms (FFT) as part of an iterative solution algorithm. Lebensohn (2001) extended this FFT-based method to the context of crystal viscoplasticity, and applied it to a number of studies (Lebensohn et al., 2005, 2008, 2009; Lee et al., 2011; Lebensohn et al., 2011; Lefebvre et al., 2012) for which the use of FEM-based approaches would have been preclusive (Prakash and Lebensohn, 2009). Very recently, an extension of this spectral method to the case of crystal elasto-viscoplasticity has been reported (Lebensohn et al., 2012; Kanjarla et al., 2012; Suquet et al., 2012; Grennerat et al., 2012), however restricted to the kinematic framework of infinitesimal strains. The feasibility of extending the FFT-based methodology to finite strains was first elaborated by Lahellec et al. (2001) for the case of composites with isotropic phases, from which the present work draws upon.

The aim of the present contribution is to merge the spectral method formulated for finite strain kinematics with a very general constitutive description of the material behavior. A flexible implementation of a material constitutive response for finite-strain crystal elasto-viscoplasticity, which can be interfaced with different FEM solvers, has been recently developed by the authors (Roters, 2011; Roters et al., 2012) and is used here to enable an unbiased comparison, both in terms of quality of the solution and computational cost, between the FE and FFT-based methods applied to full-field simulations of synthetic polycrystalline structures.

The paper is structured as follows. In Section 2 the solution strategy is described. Additional details of the simulations are given in Section 3. In Section 4 the results and performance of the proposed spectral method extension are compared to corresponding FEM simulations. We present a summary on our findings and draw our conclusions in Section 5.

## 2. Model

### 2.1. Kinematics

The deformation map  $\chi(\mathbf{x}) : \mathbf{x} \in \mathcal{B}_0 \rightarrow \mathbf{y} \in \mathcal{B}$  maps points  $\mathbf{x}$  in the reference configuration  $\mathcal{B}_0$  of a microstructural patch of interest to points  $\mathbf{y}$  in its current configuration  $\mathcal{B}$ . This deformation map can be expressed as a sum of a homogeneous deformation, characterized by a constant deformation gradient  $\bar{\mathbf{F}}$ , and a superimposed displacement fluctuation field  $\tilde{\mathbf{w}}$ ,

$$\chi(\mathbf{x}) = \bar{\mathbf{F}}\mathbf{x} + \tilde{\mathbf{w}}(\mathbf{x}), \quad (1)$$

for which periodicity conditions are enforced in the sense that  $\tilde{\mathbf{w}}^- = \tilde{\mathbf{w}}^+$  on corresponding surfaces  $\partial\mathcal{B}^-$  and  $\partial\mathcal{B}^+$ .

The total deformation gradient is given by  $\mathbf{F} = \partial\chi/\partial\mathbf{x} = \chi \otimes \nabla = \text{Grad}\chi$  and follows from Eq. (1) as the sum of the spatially homogeneous deformation gradient,  $\bar{\mathbf{F}}$ , and the locally fluctuating displacement gradient,  $\tilde{\mathbf{F}}$ , reading:

$$\mathbf{F} = \bar{\mathbf{F}} + \tilde{\mathbf{F}} \quad \text{with} \quad \tilde{\mathbf{F}} = \frac{\partial\tilde{\mathbf{w}}}{\partial\mathbf{x}} = \tilde{\mathbf{w}} \otimes \nabla = \text{Grad}\tilde{\mathbf{w}}. \quad (2)$$

### 2.2. Linear reference material

We consider the material to be governed by an arbitrary rate-dependent constitutive law that connects the deformation gradient to the first PIOLA–KIRCHHOFF stress,  $\mathbf{P}$ , at every material point in the reference configuration:

$$\mathbf{P}(\mathbf{x}) = \mathbf{f}(\mathbf{x}, \mathbf{F}, \dot{\mathbf{F}}, \mathbf{v}) \quad (3)$$

based on an evolving set of chosen internal variables  $\mathbf{v}$ .<sup>1</sup> By introducing, in the spirit of Eshelby and Mura (1987), a linear comparison material of stiffness  $\mathbb{A}$  we can reformulate the spatial heterogeneity of stress as

$$\begin{aligned} \mathbf{P}(\mathbf{x}) &= \mathbb{A}\mathbf{F}(\mathbf{x}) + \underbrace{\mathbf{P}(\mathbf{x}) - \mathbb{A}\mathbf{F}(\mathbf{x})}_{\boldsymbol{\tau}(\mathbf{x})} \\ &= \mathbb{A}\mathbf{F}(\mathbf{x}) + \boldsymbol{\tau}(\mathbf{x}) \end{aligned} \quad (4)$$

with  $\boldsymbol{\tau}(\mathbf{x})$  being the polarization field.

### 2.3. Static equilibrium

Static equilibrium (excluding body forces) with respect to the reference configuration requires (see for instance Malvern, 1969; Mura, 1987)

$$\mathbf{0} = \text{Div}\mathbf{P}(\mathbf{x}) = \text{Div}(\mathbb{A}\mathbf{F}(\mathbf{x}) + \boldsymbol{\tau}(\mathbf{x})) = \{\mathbb{A}[\chi(\mathbf{x}) \otimes \nabla] + \boldsymbol{\tau}(\mathbf{x})\} \nabla, \quad (5a)$$

<sup>1</sup> Note that a locality assumption is not required.  $\mathbf{P}$  at  $\mathbf{x}$  may be a function of more spatial locations than  $\mathbf{x}$ .

which reads, after application of the inverse FOURIER transform<sup>2</sup>

$$\mathbf{0} = \frac{1}{(2\pi)^3} \int e^{i\mathbf{k}\cdot\mathbf{x}} \{ \mathbb{A}[\boldsymbol{\chi}(\mathbf{k}) \otimes i\mathbf{k}] + \boldsymbol{\tau}(\mathbf{k}) \} i\mathbf{k} d\mathbf{k} = \mathcal{F}^{-1}(\{ \mathbb{A}[\boldsymbol{\chi}(\mathbf{k}) \otimes i\mathbf{k}] + \boldsymbol{\tau}(\mathbf{k}) \} i\mathbf{k}). \quad (5b)$$

Hence, equilibrium is fulfilled if

$$\mathbf{0} = \{ \mathbb{A}[\boldsymbol{\chi}(\mathbf{k}) \otimes i\mathbf{k}] + \boldsymbol{\tau}(\mathbf{k}) \} i\mathbf{k},$$

which is equivalent to

$$\begin{aligned} \mathbb{A}[\boldsymbol{\chi}(\mathbf{k}) \otimes \mathbf{k}] \mathbf{k} &= \boldsymbol{\tau}(\mathbf{k}) i\mathbf{k} \\ \mathbf{A}(\mathbf{k}) \boldsymbol{\chi}(\mathbf{k}) &= \boldsymbol{\tau}(\mathbf{k}) i\mathbf{k} \quad \text{for all } \mathbf{k} \neq \mathbf{0} \end{aligned} \quad (6)$$

with the so-called ‘acoustic tensor’  $\mathbf{A}(\mathbf{k})$  being introduced as shorthand notation and defined such that  $\mathbf{A}(\mathbf{k}) \mathbf{a} = \mathbb{A}[\mathbf{a} \otimes \mathbf{k}] \mathbf{k}$ . The equilibrium deformation field (in FOURIER space) is consequently found to be

$$\boldsymbol{\chi}(\mathbf{k}) = \begin{cases} \mathbf{A}(\mathbf{k})^{-1} \boldsymbol{\tau}(\mathbf{k}) i\mathbf{k} & \text{if } \mathbf{k} \neq \mathbf{0} \\ \boldsymbol{\chi}(\mathbf{0}) & \text{if } \mathbf{k} = \mathbf{0}. \end{cases} \quad (7)$$

The deformation gradient field is straightforwardly derived from this result as

$$\mathbf{F}(\mathbf{k}) = \begin{cases} -\mathbf{A}(\mathbf{k})^{-1} \boldsymbol{\tau}(\mathbf{k}) (\mathbf{k} \otimes \mathbf{k}) & \text{if } \mathbf{k} \neq \mathbf{0}, \\ \bar{\mathbf{F}} & \text{if } \mathbf{k} = \mathbf{0}, \end{cases} \quad (8)$$

with the shorthand notation  $\Gamma(\mathbf{k}) = \mathbf{A}(\mathbf{k})^{-1} \square(\mathbf{k} \otimes \mathbf{k})$  using a tensor product as defined in Appendix A. The ‘Gamma operator’  $\Gamma$  of Eq. (8) is identical to the one introduced in component form by Lhellec et al. (2001).

Since the polarization field  $\boldsymbol{\tau}$  depends on  $\mathbf{F}$  (see Eq. (4)) the implicit Eq. (8) has to be solved iteratively.

## 2.4. Numerical algorithm

A periodic hexahedral volume element with side lengths  $d_x, d_y, d_z$  is discretized into a regular grid of  $N_x \times N_y \times N_z = N$  points. The volume element has to satisfy static equilibrium as well as the external boundary conditions applied during a given period of time that is subdivided into consecutive increments. At each increment an iterative strategy is employed until both of these conditions are met within a given level of tolerance. An overview of the algorithm is presented in Appendix C and explained in more detail in the following.

### 2.4.1. Boundary conditions

Within a single time increment of  $\Delta t$  the volume element is subjected to a set of complementary boundary<sup>3</sup> conditions (BCs) in terms of deformation rate  $\dot{\mathbf{F}}_{\text{BC}}$  and stress  $\mathbf{P}_{\text{BC}}$ .<sup>4</sup> Components of both are mutually exclusive and, when not defined, set to zero in the following. These mixed boundary conditions are translated into pure deformation boundary conditions at iteration  $n + 1$  by setting

$$\{ \mathbf{F}_{\text{BC}} \}_{n+1} = \{ \bar{\mathbf{F}} \}_0 + \dot{\mathbf{F}}_{\text{BC}} \Delta t - \left\{ \frac{\partial \bar{\mathbf{F}}}{\partial \mathbf{P}} \right\}_n (\{ \bar{\mathbf{P}} \}_n - \mathbf{P}_{\text{BC}}), \quad (9)$$

where the subscript 0 indicates quantities at the beginning of the increment. The last term in Eq. (9) corrects for deviations from the prescribed stress boundary conditions. The average compliance  $\partial \bar{\mathbf{F}} / \partial \bar{\mathbf{P}}$  required for this is calculated as follows: (i) spatially average the tangent modulus  $\partial \mathbf{P} / \partial \mathbf{F}$  known at each grid point; (ii) transform the fourth-order tensor  $\langle \partial \mathbf{P} / \partial \mathbf{F} \rangle$  into a  $9 \times 9$  matrix; (iii) drop all rows  $ij$  and columns  $kl$  for which no stress boundary conditions are defined at  $ij$  or  $kl$ ; (iv) invert the reduced square matrix; (v) re-insert zero-filled rows and columns at  $ij$  and  $kl$  that were dropped before; (vi) transform the  $9 \times 9$  matrix back to a regular fourth-order tensor.

### 2.4.2. Static equilibrium using spectral method

Inserting the definition of the polarization field given by Eq. (4) into Eq. (8) and transforming back to real space yields

$$\begin{aligned} \tilde{\mathbf{F}}(\mathbf{x}) &= -\Gamma(\mathbf{x}) * [\mathbf{P}(\mathbf{F}(\mathbf{x})) - \mathbb{A}\mathbf{F}(\mathbf{x})] \\ &= -\Gamma(\mathbf{x}) * \mathbf{P}(\mathbf{F}(\mathbf{x})) + \underbrace{\Gamma(\mathbf{x}) * [\mathbb{A}\mathbf{F}(\mathbf{x})]}_{\tilde{\mathbf{F}}(\mathbf{x})} \\ &= -\Gamma(\mathbf{x}) * \mathbf{P}(\mathbf{F}(\mathbf{x})) + \tilde{\mathbf{F}}(\mathbf{x}). \end{aligned} \quad (10)$$

<sup>2</sup> Quantities in real space and FOURIER space are distinguished by notation  $Q(\mathbf{x})$  and  $Q(\mathbf{k})$ , respectively, with  $\mathbf{x}$  the position in real space,  $\mathbf{k}$  the frequency vector in FOURIER space, and  $i^2 = -1$ .  $\mathcal{F}^{-1}$  denotes inverse FOURIER transform.

<sup>3</sup> The term ‘boundary’ is here not used in its literary sense, since the periodicity inherent to the spectral method actually only allows to specify conditions that are fulfilled in a volume-averaged sense. Hence, speaking of ‘volume conditions’ might be more appropriate but was not introduced to avoid additional nomenclature.

<sup>4</sup> Stress boundary conditions must not allow for rigid body rotations.

The last simplification,  $\mathbb{F}(\mathbf{x}) * [\mathbb{A}\mathbf{F}(\mathbf{x})] \equiv \tilde{\mathbf{F}}(\mathbf{x})$ , introduced in Eq. (10) is based on the assumption that the properties of  $\mathbb{F}$  in the finite strain case are analogous to that of the infinitesimal strain case given by Michel et al. (2001). Eq. (10) can be solved by an iterative fix-point scheme to update the deformation gradient field at iteration  $n + 1$  as

$$\{\mathbf{F}(\mathbf{x})\}_{n+1} = \{\mathbf{F}(\mathbf{x})\}_n - \mathcal{F}^{-1} \left( \begin{cases} \mathbb{F}(\mathbf{k}) \{\mathbf{P}(\mathbf{k})\}_n & \text{if } \mathbf{k} \neq \mathbf{0}, \\ \{\tilde{\mathbf{F}}\}_n - \{\mathbf{F}_{\text{BC}}\}_{n+1} & \text{if } \mathbf{k} = \mathbf{0}, \end{cases} \right) \quad (11)$$

which is the basis for the updated constitutive response  $\{\mathbf{P}(\mathbf{x})\}_{n+1}$  in the next iteration. A sufficient condition for the convergence of such a scheme is that the spectral radius of its operator is  $< 1$ . For the case of isotropic elasticity, Michel et al. (2001) could show that stability is guaranteed when setting the reference stiffness  $\mathbb{A}$  to the mean of the highest and lowest stiffness value from the domain. In our situation of anisotropic elasto-plasticity, however, it is difficult to find an analogous procedure. For that reason, we choose the volume average of elastic stiffnesses over the entire domain as our reference stiffness:

$$\mathbb{A} = \langle \mathbb{C}(\mathbf{x}) \rangle. \quad (12)$$

With this choice, it turns out that the fix-point scheme converges within a reasonable number of iterations.

### 2.4.3. Convergence criterion

The refinement of  $\mathbf{F}(\mathbf{x})$  through iterating Eq. (11) brings the divergence of the associated stress field  $\mathbf{P}(\mathbf{x})$  closer to zero. Convergence of the stress-divergence field,  $\mathbf{P}(\mathbf{x}) \nabla$ , to zero is checked by requiring an associated energy term to reduce below a given threshold. Using PARSEVAL'S theorem, this energy can be conveniently formulated for a discrete FOURIER transform as

$$\frac{1}{N} \sum_{j=1}^N |\mathbf{P}(\mathbf{x}_j) \nabla|^2 = \frac{1}{N^2} \sum_{j=1}^N |\mathbf{P}(\mathbf{k}_j) i \mathbf{k}_j|^2. \quad (13)$$

Relating the square root of Eq. (13), i.e., the root mean square (RMS) of the divergence of stress, to the magnitude of the average stress we arrive at the convergence criterion

$$\varepsilon_{\text{eq}} \times m \geq \frac{\text{RMS}(\text{Div} \mathbf{P}(\mathbf{x}))}{\|\bar{\mathbf{P}}\|_2} = \frac{\sqrt{\sum_{j=1}^N |\mathbf{P}(\mathbf{k}_j) i \mathbf{k}_j|^2 / N^2}}{\|\mathbf{P}(\mathbf{0})\|_2}, \quad (14)$$

where  $\varepsilon_{\text{eq}}$  is the equilibrium tolerance. This criterion is the same as that proposed by Moulinec and Suquet (1998), but here properly scaled by the unit of length (m).

A second (relative) convergence criterion, which is evaluated in addition to Eq. (14), is used to ensure the fulfillment of potential stress boundary conditions:

$$\varepsilon_{\text{BC}} \geq \frac{\|\mathbf{P}_{\text{BC}} - \bar{\mathbf{P}}^*\|_2}{\|\bar{\mathbf{P}}\|_2} \quad \text{where} \quad \bar{P}_{*ij} = \begin{cases} 0 & \text{if } P_{\text{BC}ij} \text{ not prescribed} \\ \bar{P}_{ij} & \text{otherwise} \end{cases} \quad (15)$$

where  $\varepsilon_{\text{BC}}$  is the boundary condition tolerance.

## 3. Simulation details

### 3.1. Simulation codes

The present work uses a material model implementation from the open source Düsseldorf Advanced Material Simulation Kit (DAMASK). DAMASK provides various constitutive models that are interfaced to the newly developed spectral method solver based on the above algorithm, as well as to commercial finite element solvers. Here, MSC.Marc 2010 with the HYPELA2 user material interface was used for finite element simulations. Eight-noded hexahedral finite elements with linear shape functions (i.e. eight GAUSS integration points) were employed. For simplicity, the same regular grid generated for the spectral method was used as the FEM mesh, although the result quality might not be as good as for a locally refined and/or boundary shape-conforming mesh (Diard et al., 2005).

### 3.2. Material model and constitutive description of crystal plasticity

An exemplary material model that relates  $\bar{\mathbf{F}}$  to  $\mathbf{P}$  is chosen from DAMASK and used for both, the spectral method and finite element solution of the mechanical boundary value problem. The conceptual details of this material model are given in Roters et al. (2010). In short, the overall deformation is multiplicatively decomposed at the material point level as  $\mathbf{F} = \mathbf{F}_e \mathbf{F}_p$  into an elastic,  $\mathbf{F}_e$ , and plastic part,  $\mathbf{F}_p$ . The (SECOND PIOLA-KIRCHHOFF) stress in the intermediate configuration,  $\mathbf{S} = \mathbb{C}(\mathbf{F}_e^T \mathbf{F}_e - \mathbf{I})/2$ , depends via the anisotropic elastic stiffness  $\mathbb{C}$  on the elastic stretch. The rate of change in plastic deformation is driven by  $\mathbf{S}$  and follows from the plastic velocity gradient  $\mathbf{L}_p = \dot{\mathbf{F}}_p \mathbf{F}_p^{-1}$ . Since the exact nature of the underlying crystal plasticity law is not essential to the present work, we adopt the simple and widely known phenomenological description

of Peirce et al. (1982) for face-centered cubic crystals. Thus, the microstructure is parameterized in terms of a slip resistance  $s^\alpha$  on each of the 12  $\{111\}\langle\bar{1}10\rangle$  slip systems, which are indexed by  $\alpha = 1, \dots, 12$ . These resistances evolve asymptotically towards  $s_\infty^\alpha$  with shear  $\gamma$  according to the relationship

$$\dot{s}^\alpha = h_0 (1 - s^\alpha/s_\infty^\alpha)^w h_{\alpha\beta} \dot{\gamma}^\beta \quad (16)$$

with implicit summation over repeated indices  $\beta = 1, \dots, 12$ . Given a set of current slip resistances, shear on each system evolves at a rate of

$$\dot{\gamma}^\alpha = \dot{\gamma}_0 \left| \frac{\tau^\alpha}{s^\alpha} \right|^n \text{sgn}(\tau^\alpha), \quad (17)$$

with  $\tau^\alpha = \mathbf{S} \cdot (\mathbf{b}^\alpha \otimes \mathbf{n}^\alpha)$ . The superposition of shear on all slip systems in turn determines the plastic velocity gradient

$$\mathbf{L}_p = \dot{\gamma}^\alpha \mathbf{b}^\alpha \otimes \mathbf{n}^\alpha, \quad (18)$$

where  $\mathbf{b}^\alpha$  and  $\mathbf{n}^\alpha$  are unit vectors along the slip direction and slip plane normal, respectively. The values used for all material parameters are listed in Table 1.

### 3.3. Convergence criteria

All FEM simulations use a convergence criterion based on relative nodal force residua. For the heterogenous material response reported in Section 4.2 three different tolerances are employed and result in convergence essentially being reached in either one, two, or four iterations per increment. The spectral solver uses the convergence criteria described in Section 2.4.3 with fixed  $\varepsilon_{\text{BC}} = 0.01$  and varying  $\varepsilon_{\text{eq}}$  for comparison to the FEM results.

### 3.4. Application of periodic mixed boundary conditions

Periodicity of the solution is inherent to the spectral method due to the FOURIER approximation of the deformation gradient field. In FEM a periodic displacement field is enforced by linking the degrees of freedom for matching nodes on opposite faces. The components of the volume-averaged displacement gradient  $\bar{\mathbf{F}}$  are controlled by either directly prescribing the corresponding terms of  $\bar{\mathbf{F}}$  in case of the spectral method, or, in case of FEM, by prescribing the motion of the three control nodes at  $(d_x, 0, 0)$ ,  $(0, d_y, 0)$ , and  $(0, 0, d_z)$  with the node at  $(0, 0, 0)$  being fixed.

## 4. Results

In the following we want to directly compare the large-strain finite element method with the proposed spectral method as valid solution strategies for static equilibrium and compatibility in a periodic volume element representing a polycrystal. First, the equivalence of the material model employed in both schemes is demonstrated using unidirectional compression of a single crystal as example. Next, we compare both solution strategies at various mesh/grid resolutions of a periodic VORONOI grain structure under simple shear. The predicted average and local mechanical responses are contrasted and discussed in terms of the fulfillment of compatibility and static equilibrium. The section closes by comparing the computational effort spent in solving the problem by both methods.

### 4.1. Unidirectional compression of single crystal

To confirm the equivalence of the material model used in both methods we present results on two single crystal compression tests. Case (a) is a highly symmetric ‘cube’ orientation with Bunge (1982) Euler angles of  $\varphi_1 = 0^\circ$ ,  $\phi = 0^\circ$ ,  $\varphi_2 = 0^\circ$ . Case

**Table 1**  
Material parameters used in the simulations.

Property	Value	Unit
$C_{11}$	$106.75 \times 10^9$	Pa
$C_{12}$	$60.41 \times 10^9$	Pa
$C_{44}$	$28.34 \times 10^9$	Pa
$\dot{\gamma}_0$	$1 \times 10^{-3}$	$\text{m s}^{-1}$
$s_0$	$31 \times 10^6$	Pa
$s_\infty$	$63 \times 10^6$	Pa
$h_0$	$75 \times 10^6$	Pa
Coplanar $h_{\alpha\beta}$	1	
Non-coplanar $h_{\alpha\beta}$	1.4	
$n$	20	
$w$	2.25	

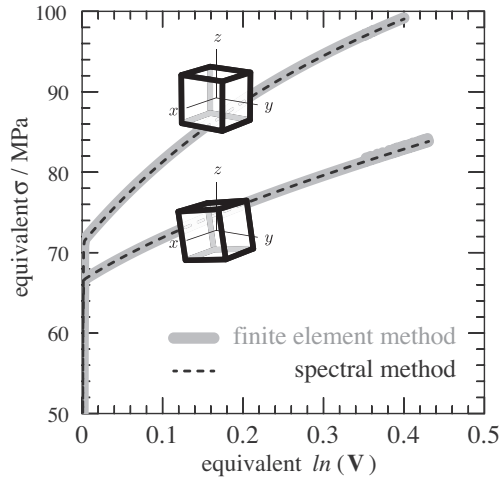


**Fig. 1.** Comparison of the mechanical response of fcc single crystals under compression along  $z$  in terms of the equivalent von Mises stress and left logarithmic strain. Overlays show crystal unit cell in loading coordinate frame.

(b) loses symmetry along the  $y$ -direction due to a small rotation by  $\phi = 10^\circ$  around the  $x$ -direction compared to (a). The periodic volume element is taken as a cube of initial dimensions  $d_{x,0} = d_{y,0} = d_{z,0} = d = 1$  m (where m can be considered as an arbitrary unit of length), discretized by  $8 \times 8 \times 8$  voxels. The boundary conditions chosen to represent compression along the  $z$ -direction are

$$\frac{\dot{\mathbf{F}}}{10^{-3} \text{ s}^{-1}} = \begin{bmatrix} * & * & * \\ 0 & * & * \\ 0 & 0 & \frac{d_z}{d_{z,0}} \end{bmatrix} \quad \text{and} \quad \frac{\mathbf{P}}{\text{Pa}} = \begin{bmatrix} 0 & 0 & 0 \\ * & 0 & 0 \\ * & * & * \end{bmatrix} \quad (19)$$

with “\*” denoting components for which complementary conditions are prescribed. These conditions are applied for 400 s in 400 equal increments resulting in a final  $z$ -compression of 0.4.

The resulting von Mises stress curves are plotted (Fig. 1) as function of the von Mises equivalent of the logarithmic left stretch tensor  $\ln \mathbf{V} = \ln(\mathbf{F}\mathbf{R}^{-1}) = (\ln \lambda_i) \mathbf{v}_i \otimes \mathbf{v}_i$ , with  $\lambda_i, \mathbf{v}_i$  being the eigenvalues and eigenvectors of  $\mathbf{V}$ . The plot shows that both schemes yield identical solutions, with the symmetric cube orientation of case (a) exhibiting a higher flow stress and hardening rate compared to the slightly rotated case (b), i.e. a behavior as expected from a straightforward Schmid factor analysis.

Fig. 2 compares the shape changes resulting from the finite element and spectral methods, at the final deformation of  $F_{zz} = 0.67$  for cases (a) and (b) in yellow and blue, respectively. Again, both methods predict identical results, which are homogeneous and fully symmetric in case (a) and nonsymmetric in case (b). This comparison demonstrates the strict equivalence of the material models employed in the two solution schemes, being the prerequisite to the evaluations performed in the following sections.

#### 4.2. Simple shear of a periodic aggregate of 50 grains

The periodic Voronoi tessellation of 50 seed points placed at random is shown in Fig. 3. All voxels belonging to one cell/crystallite are assigned the same random orientation. The physical dimensions of the cubic volume element is set to  $d^3 = 1 \times 1 \times 1 \text{ m}^3$  for simplicity. Different mesh/grid resolutions of  $16^3, 32^3, 64^3, 128^3$ , and  $256^3$  are compared.<sup>5</sup> The boundary conditions chosen to reflect simple shear along the  $y$ -direction in the  $yz$ -plane are

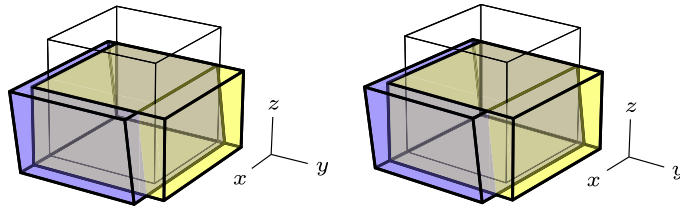
$$\frac{\dot{\mathbf{F}}}{10^{-3} \text{ s}^{-1}} = \begin{bmatrix} * & * & * \\ 0 & * & 1 \\ 0 & 0 & * \end{bmatrix} \quad \text{and} \quad \frac{\mathbf{P}}{\text{Pa}} = \begin{bmatrix} 0 & 0 & 0 \\ * & 0 & * \\ * & * & 0 \end{bmatrix} \quad (20)$$

with “\*” denoting components for which complementary conditions are prescribed. These conditions are applied for 200 s in 200 uniform increments, thus reaching a final shear of 0.2.

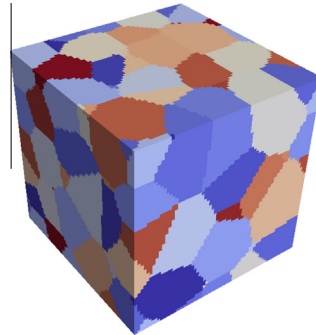
##### 4.2.1. Average response

Fig. 4 presents the volume-averaged response of the grain aggregate in terms of the shear deformation gradient component  $\bar{F}_{yz}$  as a function of the first Piola–Kirchhoff shear stress component  $\bar{P}_{yz}$ , up to the final shear of 0.2. The three upper (red)

<sup>5</sup> Resolutions of  $128^3$  and  $256^3$  were only feasible when using the spectral method.



**Fig. 2.** Final shape change of two differently oriented fcc single crystals under compression along  $z$  using FEM (left) and spectral method (right). Original volume is illustrated by hollow cube. A  $(0^\circ, 0^\circ, 0^\circ)$  orientation results in symmetric deformation (yellow). Crystal inclination by  $\phi = 10^\circ$  (about  $x$ ) renders extension along the  $y$ -direction more difficult, resulting in skewed deformation (blue). The two views can be used as a stereo pair to confirm that FEM and spectral method results coincide. (For interpretation of the references in colour in this figure legend, the reader is referred to the web version of this article.)



**Fig. 3.** Periodic Voronoi tessellation of 50 randomly placed seeds at mesh/grid resolution of  $64^3$ . Each color represents one Voronoi cell of randomly-chosen but constant crystal orientation.

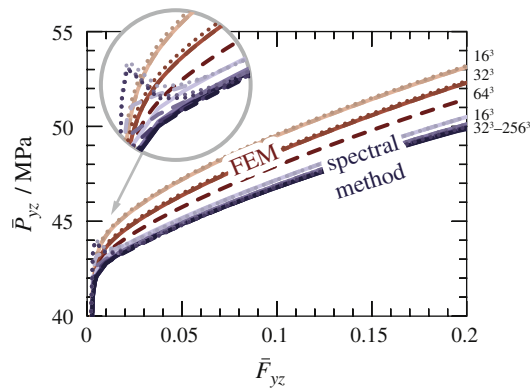


**Fig. 4.** Volume averaged shear stress  $\bar{P}_{yz}$  as function of shear deformation  $\bar{F}_{yz}$ . Mesh/grid resolution increases from light to dark colors:  $16^3$  to  $64^3$  (finite element method, upper red curves) and  $16^3$  to  $256^3$  (spectral method, lower blue curves). Convergence tolerance decreases from dotted to dashed to solid lines, all essentially coinciding. (For interpretation of the references in colour in this figure legend, the reader is referred to the web version of this article.)

sets of curves represent solutions of the finite element simulations, while the five lower (blue) sets of curves correspond to the spectral method results. Mesh/grid resolution is indicated at the right of Fig. 4 and increases with increasing darkness of each curve set. The respective convergence tolerance decreases in the order: dotted, dashed, solid.

It is seen that lower convergence tolerances do not alter the average response of the grain aggregate to a significant degree. The exception being the initial elastic–plastic transition (up to about 0.02 shear deformation) for which the spectral method markedly overpredicts the stress in case of very low precision requirements (see blue dotted curves in Fig. 4).

Regarding the overall influence of mesh/grid refinement, FEM predicts consistently higher stresses and exhibits a much more pronounced decrease in stress with increasing mesh resolution than the corresponding spectral solutions. The latter method reaches a practically converged average response already at a grid resolution of  $32^3$ . The FEM predictions, on the other hand, continuously soften with increasing resolution and are likely to eventually converge very close to the response given by the spectral method solution.

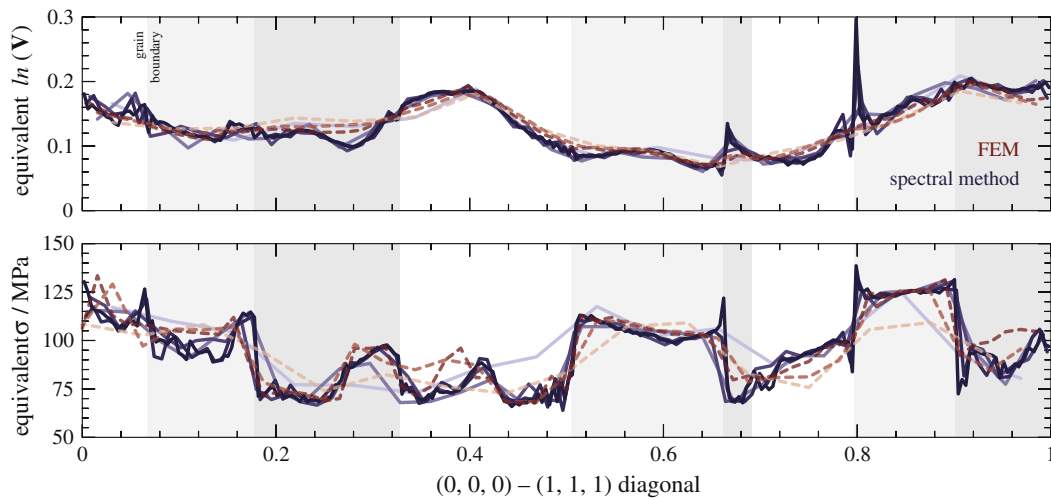


**Fig. 5.** Local response in terms of  $\text{vON Mises}$  equivalent strain (top) and stress (bottom) along a volume element diagonal after average shear deformation of  $\bar{F}_{yz} = 0.2$ . Background shading illustrates spatial extent of the nine different grains traversed. Solid (blue) and dashed (red) lines correspond to spectral method and finite element method results, respectively. Mesh/grid resolution increases with increasing darkness of curves (spectral method:  $16^3$ ,  $32^3$ ,  $64^3$ ,  $128^3$ ,  $256^3$ ; FEM:  $16^3$ ,  $32^3$ ,  $64^3$ ). (For interpretation of the references in colour in this figure legend, the reader is referred to the web version of this article.)

#### 4.2.2. Local response

In this section, the fields of local stress, deformation, and lattice rotation resulting from both methods are compared in a spatially-resolved manner. Due to the use of linear eight-noded hexahedral finite elements, the number of material points considered in FEM simulations is always eight times larger than the corresponding spectral method simulation, for a given mesh/grid resolution. Therefore, to work with the same number of point values, a reduction is performed for the deformation gradient field and the lattice rotation field by averaging the values at the eight integration points per finite element. Stress field values in FEM are nodal averages resulting after extrapolating the integration point data to the element nodes.

**4.2.2.1. Results along a volume element's diagonal.** In Fig. 5 the  $\text{vON Mises}$  equivalent strain (top) and stress (bottom) at an average shear deformation of  $\bar{F}_{yz} = 0.2$  is followed along the  $(0,0,0)$ – $(1,1,1)$  diagonal of the grain aggregate passing through nine<sup>6</sup> different grains. The profiles resulting at different mesh/grid resolutions exhibit similar trends as already observed for the volume averaged mechanical response.

Considering the equivalent strain in Fig. 5 (top), the FEM results gradually approach, at increasing mesh resolution, the profile to which the spectral method appears to have converged already at a grid resolution of  $64^3$  (third-lightest shade of blue in Fig. 5). With regard to the stress profiles in Fig. 5 (bottom), the spectral solutions can again be considered converged for resolutions exceeding  $64^3$ . Contrarily, no clear convergence trend is observed in the FEM solutions, except for its general trend towards the final spectral values.

Moreover, the strain profiles predicted by FEM are comparably smooth, while the spectral solutions show considerably higher in-grain variability. Relatively large amplitudes of high-frequency strain oscillations are found in the spectral solutions, particularly at some grain boundaries, e.g. close to diagonal coordinates of 0.8 and 0.9 in Fig. 5. At most of the grain boundaries crossed by this particular diagonal, the converged spectral results reveal significant and sudden jumps in equivalent stress. This feature is also suggested by extrapolating the evolution of FEM profiles with mesh resolution, despite them not reaching the high fidelity of the spectral profiles.

**4.2.2.2. Full-field.** Next, three-dimensional views of the resulting field quantities are presented. To reconstruct the deformed configuration illustrated in Figs. 6–8 we follow the method described in Appendix B to calculate the displacement field by integration of the deformation gradient field.

The local shear deformation gradient  $F_{yz}$ , the corresponding first  $\text{PIOLA-KIRCHHOFF}$  stress  $P_{yz}$ , and the crystal lattice reorientation resulting from the FEM and spectral method simulations are contrasted in Figs. 6–8(a) and 6–8(b), respectively, at an average shear deformation of  $\bar{F}_{yz} = 0.2$ . The three pairs in the two columns on the left of Figs. 6–8 allow us a direct comparison between FEM (leftmost, red wireframe) and spectral (central, blue wireframe) predictions, up to their maximum common mesh/grid resolution of  $64^3$ . In the rightmost column, the sequence of increasing resolution is continued, from bottom to top, for the spectral simulations.

For all three visualized field quantities, the spectral method results exhibit a small but noticeable high-frequency fluctuation that is inherent to the necessary representation (and the unavoidable truncation at high frequencies) of the micromechanical

<sup>6</sup> The thinnest grain (4th from the right in Fig. 5) is only resolved above  $32^3$ .

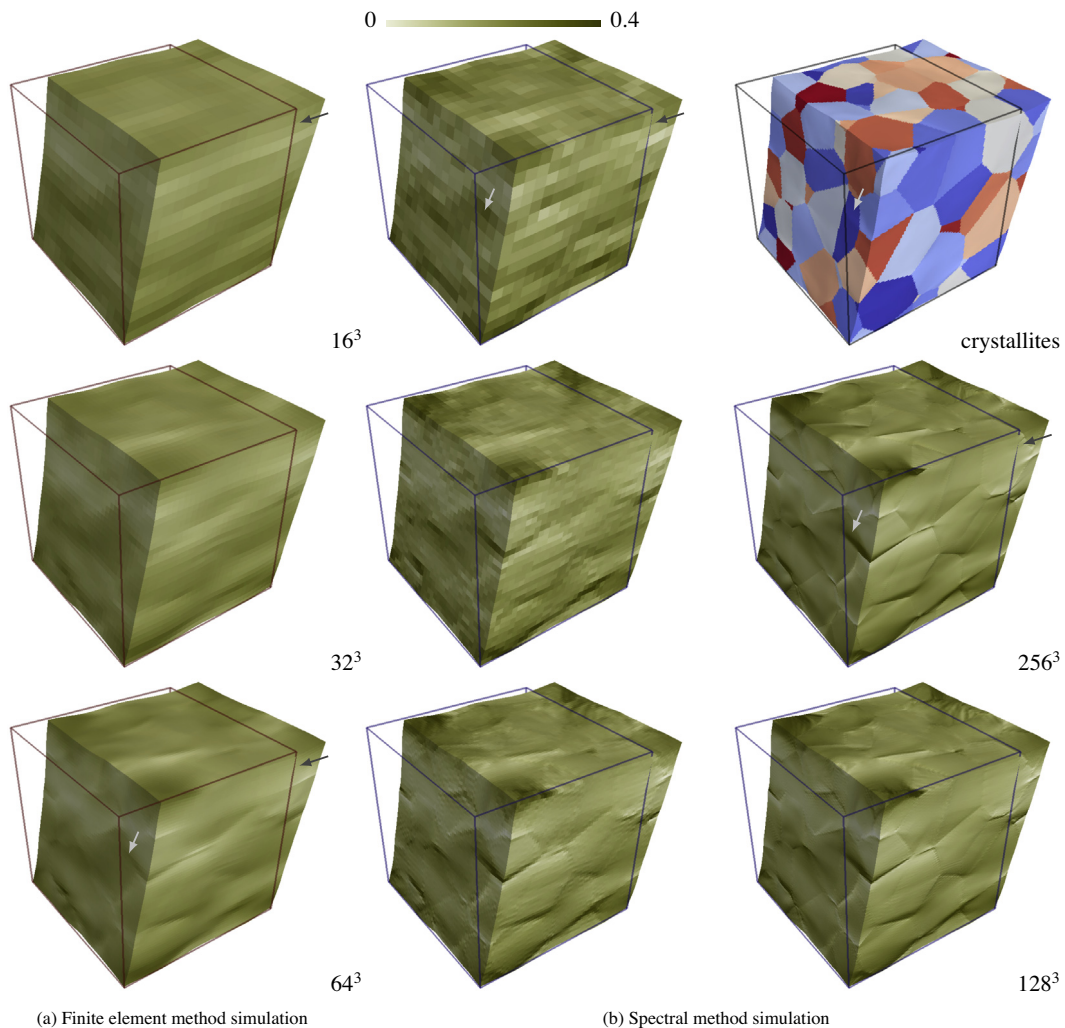


**Fig. 6.** Local shear deformation gradient  $F_{yz}$  at average shear deformation of  $\bar{F}_{yz} = 0.2$  mapped onto deformed configuration. Light arrow: intense shear emanating from close to a horizontal grain boundary into neighboring grains. Dark arrow: geometry evolution in FEM in contrast to essentially constant geometry for spectral method.

fields in FOURIER space. These fluctuations are most easily discernible at the highest spatial resolutions, *i.e.*,  $128^3$  and  $256^3$  (right column of Figs. 6–8).

The overall spatial variability of each spectral method solution is appreciably larger than that of the corresponding FEM at a given mesh/grid resolution—most obviously with respect to deformation (see Fig. 6). This, however, seems not to be predominantly related to the aforementioned high-frequency numerical fluctuations, but be a feature of the actual solutions. A typical example for this characteristic is the area of high shear deformation emanating from close to a grain boundary into two neighboring grains (see light arrows in Fig. 6). The spectral method solutions reveal this region of intense localized deformation (and many more, close to other grain boundaries) already from the lowest resolution, while the FEM solutions only start to suggest the true intensity of such features at the  $64^3$  discretization.

It is noteworthy that the spectral solutions are qualitatively the same from the lowest grid resolution on, and change quantitatively only to a small extent, owing to finer details being captured at higher spatial resolutions. This can clearly be seen when following the evolution of the deformed geometry with grid resolution. On the other hand, the FEM solutions, for example, only start to show a protrusion of the right vertical edge in the  $64^3$  case, but not at lower resolutions (dark arrows in Fig. 6a). In contrast, all spectral method solutions show virtually identical geometries between  $16^3$  and  $256^3$  (dark arrows in Fig. 6b). The low-stress spots related to a small grain sitting close to the lower-right corner of the grain aggregate and a companion larger one above it (see arrows in Fig. 7b) may serve as another example of the consistency across resolutions of the spectral results. This persistent feature is already present in the  $16^3$  spectral case, but only starts to emerge in FEM between the  $32^3$  and  $64^3$  resolutions. Practically all features that can be observed at the  $256^3$  resolution are already discernible in the  $32^3$  spectral case. The corresponding  $32^3$  element FEM results lack fidelity and appear much more ‘blurred’.

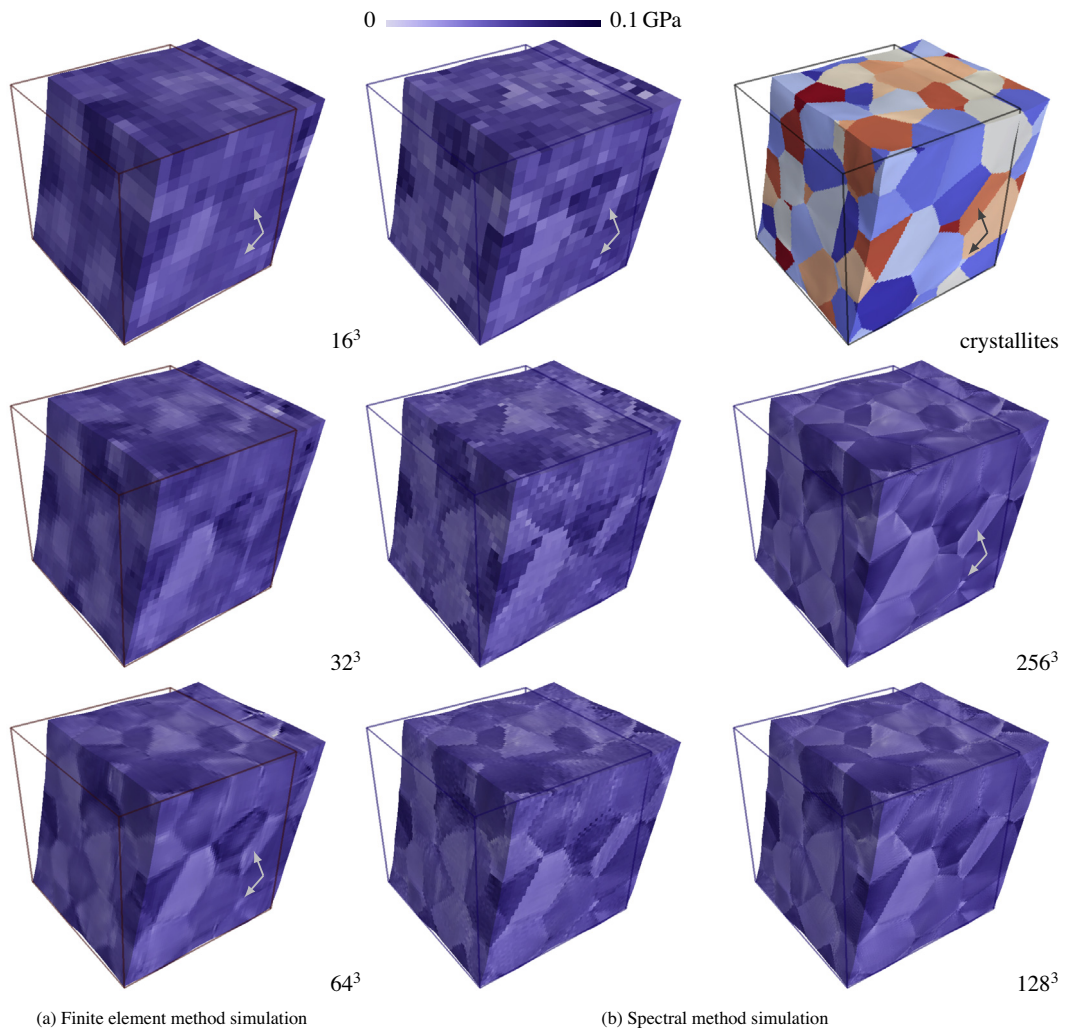


**Fig. 7.** Local first Piola–Kirchhoff shear stress  $P_{yz}$  at average shear deformation of  $\bar{F}_{yz} = 0.2$  mapped onto the deformed configuration. Arrows highlight two examples of low-stress grains within the aggregate that are captured at all resolutions for the spectral method but emerge for the FEM only at higher resolution.

In contrast to the almost stationary appearance of the spectral results, the FEM solutions exhibit a continuing evolution between resolutions  $16^3$  and  $64^3$ . A hypothetical converged FEM solution, which would require a resolution significantly larger than  $64^3$ , is likely to fall close to the most highly resolved spectral result. This, together with the other characteristics mentioned above, supports the observation that the predicted mechanical response is virtually converged for spectral calculations exceeding a resolution of about  $32^3$ , while the FEM method requires resolutions significantly larger than  $64^3$  to reach ultimate convergence.

Finally, a close inspection reveals that the spectral results show peculiar oscillations of the predicted field at some locations (for instance, within the upper left grain highlighted in Fig. 8b). These oscillations are not present in the corresponding FEM simulations and their wavelength decreases by a factor of two for each doubling of the grid resolution. The origin of these oscillations is presently not clear and will be part of a future investigation.

#### 4.2.3. Compatibility

This section compares the incompatibility of the (discrete) deformation gradient field  $\mathbf{F}(\mathbf{x})$  resulting from the FEM and spectral method simulations. We quantify incompatibility as the FROBENIUS norm of the finite-strain incompatibility tensor, *i.e.*,

$$\text{Inc} := \|\text{Curl } \mathbf{F}(\mathbf{x})\|_F = \|\mathbf{F}(\mathbf{x}) \times \nabla\|_F. \quad (21)$$

The curl of the deformation gradient field is conveniently calculated in FOURIER space as

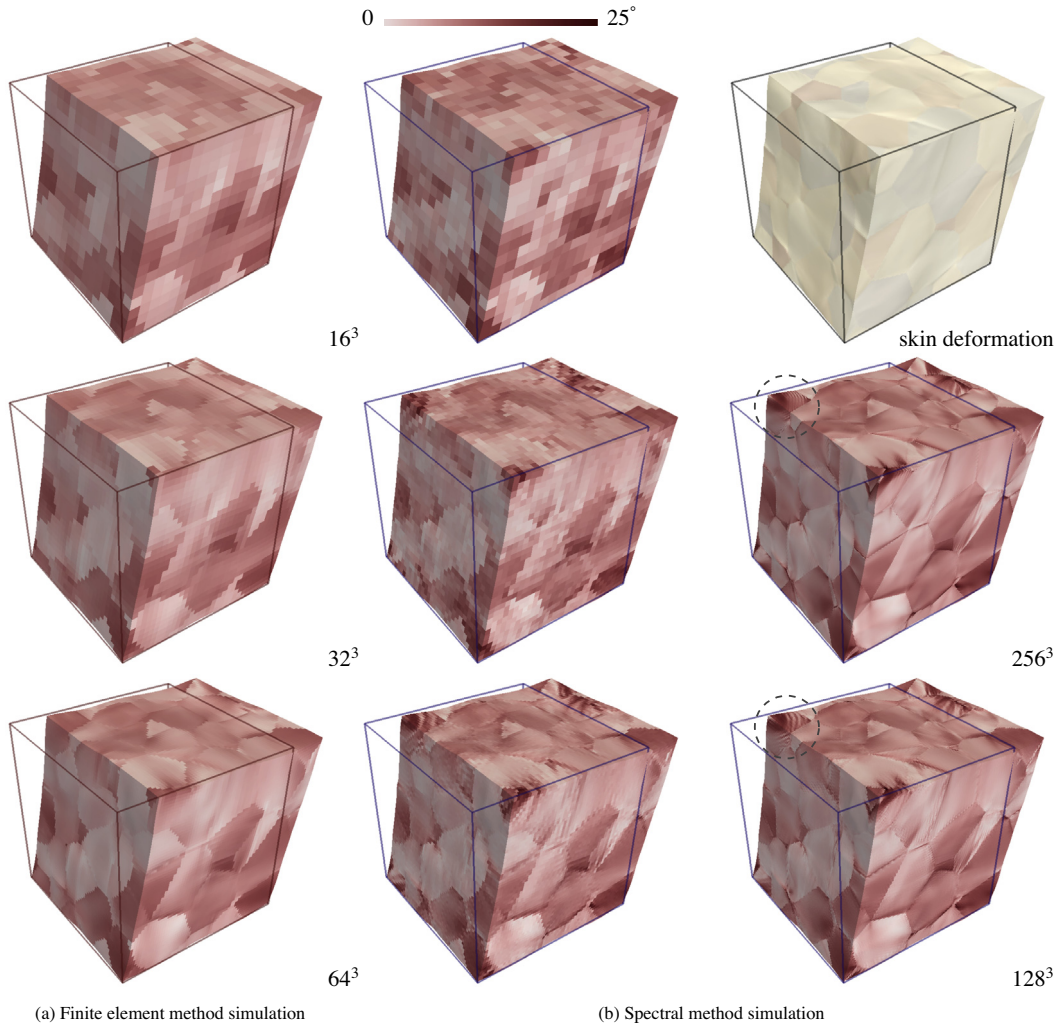


**Fig. 8.** Local rotation angle between initial and current grain orientation after average shear deformation of  $\bar{F}_{yz} = 0.2$  mapped onto the deformed configuration. Circles indicate an example of a potential artifact related to the FOURIER approximation in the spectral method.

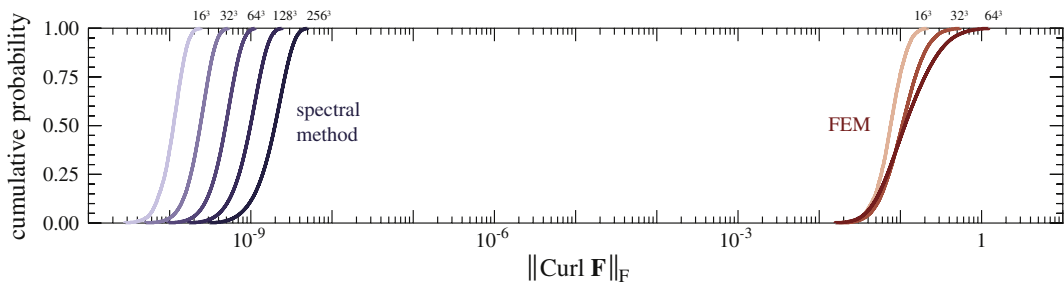


**Fig. 9.** Statistical distributions of local incompatibility for different mesh/grid resolutions at average shear deformation  $\bar{F}_{yz} = 0.2$ .

$$\text{Curl } \mathbf{F}(\mathbf{x}) = \mathcal{F}^{-1}(\mathbf{F}(\mathbf{k}) \times i\mathbf{k}). \tag{22}$$

Fig. 9 presents the distributions of incompatibility resulting from post-processing both solution methods at different mesh/grid resolutions at the final average shear deformation  $\bar{F}_{yz} = 0.2$ . These results were found to not depend noticeably on the chosen convergence tolerance. The incompatibility of the spectral results essentially equals the theoretical value of zero within numerical precision, while that of the FEM result is about 8–9 orders of magnitude larger. For the spectral

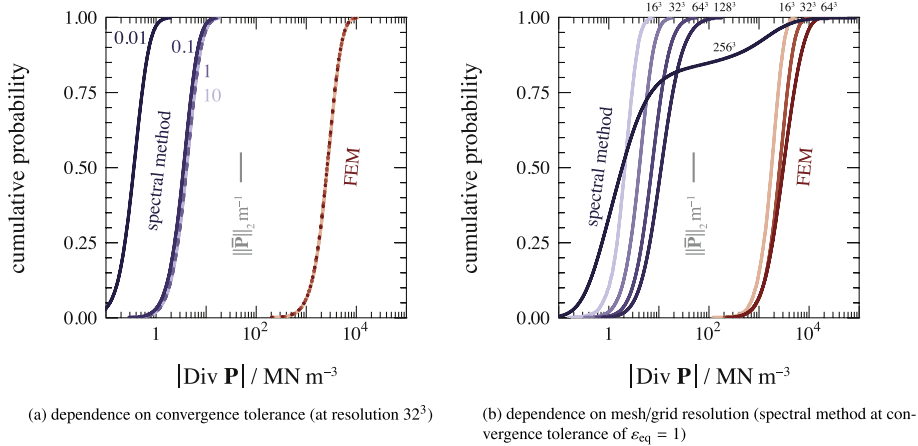


**Fig. 10.** Distribution of local first Piola–Kirchhoff stress divergence magnitudes at average shear deformation  $\bar{F}_{yz} = 0.2$  for FEM (red) and spectral method (blue). Short gray bar at  $50 \text{ MN m}^{-3}$  corresponds to a reference value of  $\|\bar{\mathbf{P}}\|_2$  divided by the longest edge of the simulated grain aggregate (1 m). (For interpretation of the references in colour in this figure legend, the reader is referred to the web version of this article.)

method, a doubling of (linear) resolution shifts the distribution to higher values by a factor of two. Obviously, the point-to-point incompatibility remains essentially unchanged with resolution, but due to the reduction of the grid spacing all values of spatial derivatives double. A slight, but not fully systematic, increase of incompatibility with increasing mesh resolution is also observed for the FEM results.

#### 4.2.4. Static equilibrium

By design, the finite element method seeks fulfillment of stress equilibrium only in an integral or ‘weak’ form. The presented spectral method, on the contrary, is set up to fulfill strong equilibrium at the discretization points (see Eq. (5)). In this section, the absolute degree to which static equilibrium is maintained in the reference configuration, *i.e.*  $\text{Div } \mathbf{P} = \mathbf{0}$ , is contrasted for both methods at the final average shear deformation  $\bar{F}_{yz} = 0.2$ . The divergence of the field of first Piola–Kirchhoff stress is conveniently<sup>7</sup> calculated in Fourier space and then transformed back to real space.

Fig. 10 compares the distribution of body force values resulting from FEM (red) and spectral method (blue) for different levels of their respective convergence criterion at constant mesh/grid resolution of  $32^3$  (a) and for different mesh/grid resolutions at constant convergence tolerance (b). The average stress  $\|\bar{\mathbf{P}}\|_2$ , divided by the longest edge of the volume element, is taken as reference magnitude and its value of  $50 \text{ MN m}^{-3}$  is indicated by a vertical gray bar in Figs. 10a and b. All resulting distributions turn out to be close to log-normal (with one exception at  $256^3$ , see Fig. 10b and below).

In the FEM simulations, three different tolerance limits for residual nodal forces were considered. Nevertheless, all three FEM distributions fall on top of each other despite performing one, two, or even four stress iterations per increment for the different tolerances (see dashed lines in Fig. 11a). The median values of FEM body force are about a factor of 50 larger than the reference magnitude (gray bar in Fig. 10a).

A different situation is found in the case of the spectral results. For the two lowest convergence tolerances of 0.01 and 0.1 the median divergence value falls very close to 0.01 and 0.1 of the reference quantity, as it would be expected from Eq. (5). For the even higher tolerances of 1 and 10, the stress equilibrium does not deteriorate any further, but a median divergence of about  $0.1 \|\bar{\mathbf{P}}\|_2 \text{ m}^{-1}$  is retained. This behavior can be easily understood in terms of the number of iterations needed to achieve stress equilibrium as plotted in Fig. 11a: With the lowest convergence tolerance, *i.e.* 0.01 as topmost line, equilibrium is reached after 13 iterations in increment 200. With the three higher tolerances only two iterations are necessary<sup>8</sup> in the final increment, hence, these three reach about the same quality in stress equilibrium (as is found in Fig. 10a).

Fig. 10b illustrates, for a given convergence tolerance, the change in the distribution of divergence values with mesh/grid resolution. For both methods, a shift to larger values with increasing resolution is found. This feature is again mainly related to the number of iterations required for convergence. In case of FEM, the (almost) constant number of iterations illustrated in Fig. 11a for the intermediate convergence tolerance are independent of resolution. In case of the spectral method, the same is true since for the tolerance of 1 all resolutions converge very similar to the  $16^3$  curve shown in Fig. 11b, *i.e.* eventually taking a constant value of two iterations. The stress field is, therefore, refined to basically the same accuracy in both methods, but the point-to-point distances in the geometry decrease with increasing resolution. The divergence, as a spatial derivative, consequently increases by roughly the increase in (linear) resolution. The one exception observed is for the highest resolution of  $256^3$ . Here, the distribution turns bimodal with a fraction of approximately 0.15 having substantially larger divergences than

<sup>7</sup> Direct numerical derivation by a finite difference scheme in real space turns out to be ambiguous. Due to the strongly heterogeneous grain structure, finite differences do not converge to a meaningful result with increasing order of accuracy.

<sup>8</sup> The minimum iteration count for the spectral method was intentionally set to a value of two.

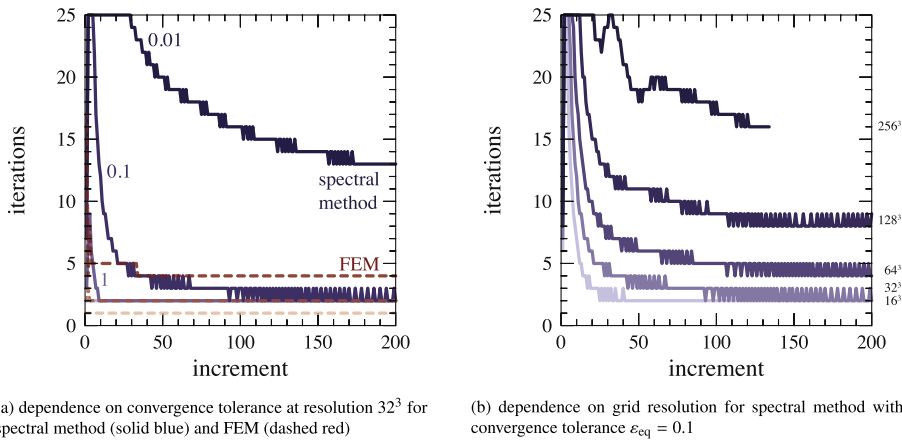


**Fig. 11.** Iterations required per increment to reach convergence. At each iteration, the constitutive response is evaluated and the boundary value problem is attempted. Spectral method is intentionally limited between 2 and 25 iterations.

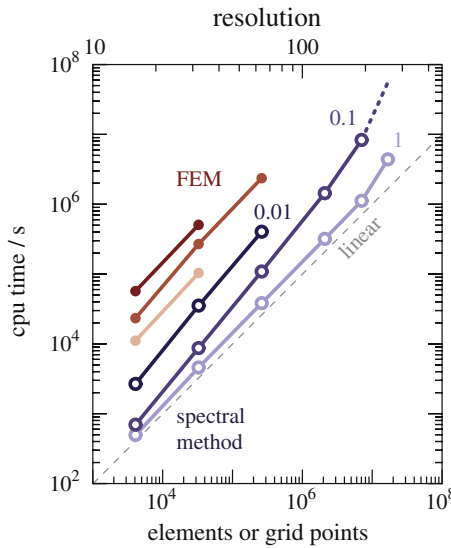


**Fig. 12.** Calculation time corresponding to simulations using FEM (red, filled circles) and spectral method (blue, open circles) at different resolutions and convergence tolerances (decreasing with increasing darkness). (For interpretation of the references in colour in this figure legend, the reader is referred to the web version of this article.)

the rest. We speculate that this response is a consequence of the spectral method strictly maintaining compatibility (see Fig. 9) at the expense of equilibrium in locations where strain deformation localization occurs. This peculiarity is currently being investigated and will be reported in a forthcoming publication.

By comparing the median body force achieved by FEM and the spectral method it is seen that the latter fulfills static equilibrium relatively better, by a factor of about  $10^3$  (depending on the convergence tolerance chosen in the spectral method).

#### 4.2.5. Computational cost

Fig. 12 summarizes the computational cost, in terms of cpu time spent on 8 cores of a dual Xeon X5670 (12 cores @ 2.93 GHz in total), for FEM and spectral method simulations, for different convergence tolerances, as a function of mesh/grid resolution.

The computation times of the FEM simulations scale proportionally with the number of elements used for discretization (being indicative of an optimal matrix inversion algorithm in the currently employed solver). The increasing number of iterations entailed by a decreasing convergence tolerance (see Fig. 11a) is directly reflected by the increase of computing times by factors of 2 and 4 relative to the lowest precision, which requires only one iteration per increment for convergence.

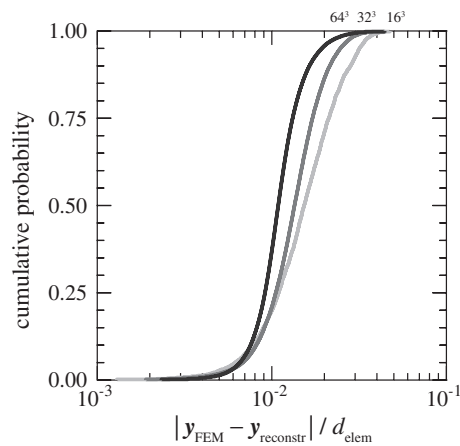


**Fig. 13.** Statistical distribution of distances, normalized by the element size  $d_{\text{elem}}$ , between displaced nodes and corresponding points obtained through reconstruction of displacement field  $\bar{\mathbf{w}}$  from deformation gradient field  $\bar{\mathbf{F}}(\mathbf{x})$  for FEM simulations. Mesh resolution increases from light to dark (right to left) from  $16^3$  to  $32^3$  to  $64^3$ .

The overall computational cost of the spectral simulations is much less and falls about 1–2 orders of magnitude below that of the corresponding FEM cost, indicating that one iteration of FEM is much more costly than one of the spectral method. Computational cost scales in direct proportion to the number of grid points, as long as the total number of iterations for convergence remains independent of resolution. This is the case of practically all simulations up to  $128^3$  elements, for convergence tolerances of 1 or larger, as they converge after two iterations per increment (Fig. 11a). Only at the highest resolution of  $256^3$  a worse-than-linear increase is observed for the converge tolerance of 1. This is related to the emergence of regions in which static equilibrium cannot be maintained as easily any more—potentially due to strongly localized deformation in their vicinity. For the tighter convergence tolerances (0.1 and 0.01) a generally worse-than-linear increase of cpu time with element count is observed. This reflects the marked increase in iterations (see Fig. 11b) that are required to satisfy  $\text{Div}\mathbf{P} = \mathbf{0}$  in strong form (see Eq. (5)).

## 5. Summary

The mechanics of polycrystals is characterized by heterogeneous fields of stress and strain, due to the intricate interactions between anisotropic grains. In order to capture this heterogeneity and predict the resulting properties at micro and macro scales, an accurate and efficient solution of the mechanical boundary-value problem is necessary. In the present work, we have formulated a spectral method capable of solving stress equilibrium and strain compatibility within a finite-strain framework, and compared its results to the standard finite element method, using the exact same material model. The equivalence of the constitutive material description was checked by simulating homogeneous single crystal deformation.

Simple shear up to 0.2 of a periodic aggregate containing 50 grains was chosen as example for a more detailed comparison of both methods. A number of observations can be made from this comparison: (i) the volume-averaged strength of the grain aggregate predicted by FEM is distinctly larger than that predicted by the spectral method. Furthermore, the strength constantly reduces with increasing mesh resolution in the FEM simulations, such that no converged response is found even at the highest resolution of  $64^3$ . In contrast, the volume-averaged mechanical response does not change significantly any more for the spectral method for mesh resolutions between  $32^3$  and  $256^3$  (see Fig. 4). (ii) The same relatively much earlier convergence with mesh resolution of the spectral method is also seen for the local fields. Virtually all features that are present in the spectral results at the highest resolution ( $256^3$ ) are already established both qualitatively as well as quantitatively at much lower resolution of  $32^3$ . The FEM, on the contrary, is at  $64^3$  still relatively far from reaching quantitative agreement with the high-resolution spectral result (see Figs. 6–8). (iii) The compatibility of the deformation gradient field as well as the static equilibrium of the stress field is fulfilled better by orders of magnitude by the spectral solutions (see Figs. 9,10). (iv) The spectral method is amenable to reach spatial resolutions that are prohibitively expensive with FEM in terms of memory requirement and—even more restrictive—in terms of computation time. In the latter respect, the spectral method is faster by about a factor of 50, resulting in roughly similar computation times for a  $64^3$  resolution FEM simulation and  $256^3$  resolution spectral simulation (see Fig. 12).

Two essential differences between the spectral and finite element methods with respect to the solution approximation and problem description appear essential to understand the above differences: Standard FEM operates on low-order (typically linear or quadratic) piecewise approximations by shape-functions within the elements that discretize the geometry. Stress equilibrium is required only in a volume-averaged (or weak) sense by indirectly requiring residual nodal forces to vanish. In contrast, the spectral method approximates the fields of stress and deformation gradient by a FOURIER series, i.e., by

superposition of as many sinusoidal functions as the number of points in the regular grid used for discretization. Furthermore, strong stress equilibrium is required at all of those discretization points.

The spectral method, originally proposed by Moulinec and Suquet (1994, 1998), extended to polycrystals by Lebensohn (2001), and now complemented by the flexible material model implemented as DAMASK, is a promising and powerful tool. The software used in this work is open-source and freely available at <http://damask.mpie.de/>. It provides the means for further investigation of important open issues related to the micromechanics of polycrystals, like damage initiation, deformation localization, micro-texture development, or nucleation of phase transformations. Another interesting application of this class of spectral methods—enabled by their fast convergence with mesh resolution—is their potential use as computational homogenization tool at the mesoscale, for relatively coarse volume elements, within multiscale approaches based on FEM at macro level.

## Acknowledgements

The authors benefitted from many fruitful discussions with Prof. Bob Svendsen and Dr. Pratheek Shanthraj. The present work was generously supported by a Humboldt Research Award and the US DOE Office of Advanced Scientific Computing Research (ASCR) through the Exascale Co-Design Center for Materials in Extreme Environments (ExMatEx) (RAL) and in part carried out under project number M41.2.10410 (MD) in the framework of the Research Program of the Materials innovation institute M2i ([www.m2i.nl](http://www.m2i.nl)). The code development was performed as part of the “Computational Mechanics of Polycrystals – CMC” initiative, a joint research group between the Max-Planck-Institut für Eisenforschung, Düsseldorf, and the Fraunhofer Institut für Werkstoffmechanik, Freiburg. The associated financial support from the Max Planck Society is gratefully acknowledged.

## Appendix A. Notation

As a general scheme of notation, vectors are written as boldface lowercase letters (e.g.  $\mathbf{a}$ ,  $\mathbf{b}$ ), second-order tensors as boldface capital letters (e.g.  $\mathbf{A}$ ,  $\mathbf{B}$ ), and fourth-order tensors as blackboard-bold capital letters (e.g.  $\mathbb{A}$ ,  $\mathbb{B}$ ). For vectors and tensors, Cartesian components are denoted as, respectively,  $a_i$ ,  $A_{ij}$  and  $A_{ijkl}$ . The action of a second-order tensor upon a vector is denoted as  $\mathbf{A}\mathbf{b}$  (in components  $A_{ij}b_j$ , implicit summation over repeated indices is used unless specified otherwise) and that of a fourth-order tensor upon a second order tensor is designated as  $\mathbb{A}\mathbf{B}$  ( $A_{ijkl}B_{kl}$ ). The composition of two second-order tensors is denoted as  $\mathbf{A}\mathbf{B}$  ( $A_{ik}B_{kj}$ ). The tensor product  $\mathbf{A}\square\mathbf{B}$  of two second-order tensors  $\mathbf{A}$  and  $\mathbf{B}$  is defined by  $(\mathbf{A}\square\mathbf{B})\mathbf{C} := \mathbf{A}\mathbf{C}\mathbf{B}$ . The tensor (or dyadic) product between two vectors is denoted as  $\mathbf{a} \otimes \mathbf{b}$  ( $a_i b_j$ ). All inner products are indicated by a single dot between the tensorial quantities of the same order, e.g.,  $\mathbf{a} \cdot \mathbf{b}$  ( $a_i b_i$ ) for vectors and  $\mathbf{A} \cdot \mathbf{B}$  ( $A_{ij} B_{ij}$ ) for second-order tensors. The cross-product of a second-order tensor  $\mathbf{A}$  with a vector  $\mathbf{a}$ , denoted by  $\mathbf{A} \times \mathbf{a}$ , is a second-order tensor defined in components as  $(\mathbf{A} \times \mathbf{a})_{ij} = A_{ik} a_l \epsilon_{lkj}$ , where  $\epsilon$  is the LEVITA–CIVITA permutation matrix. The transpose,  $\mathbf{A}^T$ , of a tensor  $\mathbf{A}$  is denoted by a superscript “T”, and the inverse,  $\mathbf{A}^{-1}$ , by a superscript “−1”.  $\|\mathbf{A}\|_2$  and  $\|\mathbf{A}\|_F$  designate the spectral norm and FROBENIUS norm of matrix  $\mathbf{A}$ , respectively. The ‘del’ operator is denoted by the nabla symbol  $\nabla$ .  $\langle \cdot \rangle$  produces the spacial average of the quantity in angle brackets. Additional notation is introduced where required.

## Appendix B. Reconstruction of displacement field from deformation gradient field

The following method was used to reconstruct the deformed polycrystal geometry for visualization in Figs. 6–8. This shape reconstruction algorithm is suitable for volume elements with periodic boundary conditions for which the deformation gradient on each point of a regular, three-dimensional grid in undeformed configuration is known. Starting from the separation of the deformation gradient in average and fluctuating part (Eq. (2)), the fluctuation in the displacement field can be recovered as

$$\tilde{\mathbf{F}}(\mathbf{x}) = \tilde{\mathbf{w}}(\mathbf{x}) \otimes \nabla,$$

$$\tilde{\mathbf{F}}(\mathbf{k}) = \tilde{\mathbf{w}}(\mathbf{k}) \otimes i\mathbf{k},$$

$$\tilde{\mathbf{F}}(\mathbf{k})i\mathbf{k} = \tilde{\mathbf{w}}(\mathbf{k})(i\mathbf{k} \cdot i\mathbf{k}),$$

$$-\tilde{\mathbf{F}}(\mathbf{k}) \frac{i\mathbf{k}}{|\mathbf{k}|^2} = \tilde{\mathbf{w}}(\mathbf{k}) \quad \forall \mathbf{k} \neq \mathbf{0}. \quad (23)$$

Since the fluctuation,  $\tilde{\mathbf{F}}$ , of the deformation gradient has by definition a vanishing average, the exclusion of the zero-frequency vector  $\mathbf{k} = \mathbf{0}$  in Eq. (23) is inconsequential. When inserting the result of Eq. (23) into Eq. (1) the overall deformation map can be assembled as

$$\mathbf{y}(\mathbf{x}) = \bar{\mathbf{F}}\mathbf{x} - \mathcal{F}^{-1} \left( \tilde{\mathbf{F}}(\mathbf{k}) \frac{i\mathbf{k}}{|\mathbf{k}|^2} \right), \quad (24)$$

i.e., integrating the locally fluctuating part of the deformation gradient in FOURIER space and the average part in real space. A beneficial side effect of this splitting is the possibility to independently rescale the displacement fluctuation in the visualization.

From Eq. (24) the coordinates of the deformed grid are recovered. For a subsequent visualization we construct hexahedral cells around these grid points. Each node of a cell is positioned at the average location of all eight surrounding grid points, accounting for periodicity.

A verification of the reconstruction accuracy is possible based on a FEM simulation result since the nodal coordinates of the FEM mesh should coincide with the positions of the cell nodes of the reconstruction mesh in the limit of infinite resolution. Fig. 13 shows the distribution of distances relative to element size  $d_{\text{elem}}$  between reconstructed node positions  $\mathbf{y}_{\text{reconst}}$  and FEM node positions  $\mathbf{y}_{\text{FEM}}$ . The data confirms the expected systematic decrease of deviations with increasing resolution. On absolute grounds, the reconstruction accuracy is very good: even for the lowest resolution of  $16^3$  the reconstructed nodal coordinates match the original positions with a median error of less than 2% of the element size.

### Appendix C. Algorithm

The algorithm used to solve for static equilibrium with the spectral method is given in pseudocode in Algorithm 1. It follows the procedure that was outlined for a single increment in Section 2.4. Here, it is extended to the general case of several load cases, each consisting of a series of increments.

We observed a noticeable improvement in convergence speed by assuming the evolution of the stress boundary conditions and of the deformation gradient field to follow in the first iteration of an increment the trajectory of the preceding converged increment. In the calculation of  $\mathbb{F}$  the reference stiffness  $\mathbb{A}$  is selected as the volume average  $\langle \mathbb{C}(\mathbf{x}) \rangle$  of all individual linear elastic stiffnesses.

#### Algorithm 1. Spectral method boundary value problem solver.

---

```

k,  $\mathbb{F}$  = Func(geometry, material);           // initialize frequency vectors and Gamma operator
for  $l \leftarrow 1$  to  $n_{\text{load\_cases}}$  do           // looping over load cases
  for  $s \leftarrow 1$  to  $n_{\text{incs}}(\text{load\_case}(l))$  do // looping over increments of current load case
     $\Delta \mathbf{F}_{\text{BC}} = \begin{cases} \text{Func}(\text{load\_case}(l)) & \forall ij \text{ where } F_{\text{BC}ij} \text{ prescribed} \\ 0 & \text{otherwise} \end{cases}$ ;           // deformation bc
     $\mathbf{P}_{\text{BC}} = \text{Func}(\text{load\_case}(l))$   $\forall ij$  where  $P_{\text{BC}ij}$  prescribed;           // stress bc
    if  $s == 1$  then // homogeneous guess for every first increment
       $\mathbf{F}_{\text{BC}} = \{\mathbf{F}_{\text{BC}}\}^{s-1} + \Delta \mathbf{F}_{\text{BC}}$ ;
       $\mathbf{F}(\mathbf{x}) = \{\mathbf{F}(\mathbf{x})\}^{s-1} + \Delta \mathbf{F}_{\text{BC}}$ ;
    else // continue along former trajectory
       $\mathbf{F}_{\text{BC}} = \begin{cases} 2\{F_{\text{BC}ij}\}^{s-1} - \{F_{\text{BC}ij}\}^{s-2} & \forall ij \text{ where } P_{\text{BC}ij} \text{ prescribed} \\ \{F_{\text{BC}ij}\}^{s-1} + \Delta F_{\text{BC}ij} & \text{otherwise} \end{cases}$ ;           // for stress bc
       $\mathbf{F}(\mathbf{x}) = 2\{\mathbf{F}(\mathbf{x})\}^{s-1} - \{\mathbf{F}(\mathbf{x})\}^{s-2}$ ;           // and for def grad field
    while  $\text{error\_stress} \geq \text{tol}$  or  $\text{error\_divergence} \geq \text{tol}$  do // convergence loop
       $\mathbf{P}(\mathbf{x}) = \text{Func}(\mathbf{F}(\mathbf{x}))$ ;           // constitutive law
       $\mathbf{F}_{\text{BC}} = \mathbf{F}_{\text{BC}} - \text{Func}\left(\overline{\mathbf{P}}, \left\{\frac{\partial \mathbf{F}}{\partial \mathbf{P}}\right\}^{s-1}\right)$ ;           // correct deformation bc
       $\mathbf{P}(\mathbf{k}) = \text{FFT}(\mathbf{P}(\mathbf{x}))$ ;           // FT of stress field
       $\mathbf{F}(\mathbf{x}) = \mathbf{F}(\mathbf{x}) - \text{FFT}^{-1}\left(\begin{cases} \mathbb{F}(\mathbf{k}) \mathbf{P}(\mathbf{k}) & \text{if } \mathbf{k} \neq \mathbf{0} \\ \overline{\mathbf{F}} - \mathbf{F}_{\text{BC}} & \text{if } \mathbf{k} = \mathbf{0} \end{cases}\right)$ ;           // update def grad field
       $\text{error\_stress} = \text{Func}(\overline{\mathbf{P}}, \text{load\_case}(l))$ ;
       $\text{error\_divergence} = \text{Func}(\mathbf{P}(\mathbf{k}), \mathbf{k})$ ;
    Result:  $\mathbf{P}(\mathbf{x}), \mathbf{F}(\mathbf{x})$ ;           // store results of converged increment

```

---

### References

- Bunge, H., 1982. Texture Analysis in Materials Science. Butterworths, London.
- Cailletaud, G., Diard, O., Feyel, F., Forest, S., 2003. Computational crystal plasticity: from single crystal to homogenized polycrystals. Techn. Mech. 23, 130–145.
- Clayton, J., McDowell, D., 2003. A multiscale multiplicative decomposition for elastoplasticity of polycrystals. Int. J. Plasticity 19, 1401–1444.
- DAMASK. Düsseldorf Advanced Material Simulation Kit. <<http://damask.mpi.de/>>.

- Delannay, L., Melchior, M., Signorelli, J., Remacle, J.F., Kuwabara, T., 2009. Influence of grain shape on the planar anisotropy of rolled steel sheets – evaluation of three models. *Comput. Mater. Sci.* 45, 739–743.
- Diard, O., Leclercq, S., Rousselier, G., Cailletaud, G., 2005. Evaluation of finite element based analysis of 3D multicrystalline aggregates plasticity. *Int. J. Plasticity* 21, 691–722.
- Grennerat, F., Montagnat, M., Castelnau, O., Vacher, P., Moulinec, H., Suquet, P., Duval, P., 2012. Experimental characterization of the intragranular strain field in columnar ice during transient creep. *Acta Mater.* 60, 3655–3666.
- Kanjarla, A., Lebensohn, R., Balogh, L., Tomé, C., 2012. Study of internal lattice strain distributions in stainless steel using a full-field elasto-viscoplastic formulation based on fast Fourier transforms. *Acta Mater.* 60, 3094–3106.
- Kim, J., Lee, M.G., Wagoner, R., 2010. A boundary smoothing algorithm for image-based modeling and its application to micromechanical analysis of multi-phase materials. *Comput. Mater. Sci.* 47, 785–795.
- Kraska, M., Doig, M., Tikhomirov, D., Raabe, D., Roters, F., 2009. Virtual material testing for stamping simulations based on polycrystal plasticity. *Comput. Mater. Sci.* 46, 383–392.
- Lahellec, N., Michel, J., Moulinec, H., Suquet, P., 2001. Analysis of inhomogeneous materials at large strains using fast Fourier transforms. In: Miehe, C. (Ed.), *Proc. IUTAM Symposium, Solid Mechanics and its Applications*, vol. 108. Kluwer Academic Publishers, Dordrecht, The Netherlands, pp. 247–258.
- Lebensohn, R., 2001. N-site modeling of a 3D viscoplastic polycrystal using Fast Fourier Transform. *Acta Mater.* 49, 2723–2737.
- Lebensohn, R., Brenner, R., Castelnau, O., Rollett, A., 2008. Orientation image-based micromechanical modelling of subgrain texture evolution in polycrystalline copper. *Acta Mater.* 56, 3914–3926.
- Lebensohn, R., Castelnau, O., Brenner, R., Gilormini, P., 2005. Study of the antiplane deformation of linear 2-D polycrystals with different microstructures. *Int. J. Solids Struct.* 42, 5441–5459.
- Lebensohn, R., Idiart, M., Castañeda, P., Vincent, P.G., 2011. Dilatational viscoplasticity of polycrystalline solids with intergranular cavities. *Philos. Mag.* 91, 3038–3067.
- Lebensohn, R., Kanjarla, A., Eisenlohr, P., 2012. An elasto-viscoplastic formulation based on fast Fourier transforms for the prediction of micromechanical fields in polycrystalline materials. *Int. J. Plasticity* 32–33, 59–69.
- Lebensohn, R., Montagnat, M., Mansuy, P., Duval, P., Meysonnier, J., Philip, A., 2009. Modeling viscoplastic behavior and heterogeneous intracrystalline deformation of columnar ice polycrystals. *Acta Mater.* 57, 1405–1415.
- Lee, S.B., Lebensohn, R., Rollett, A., 2011. Modeling the viscoplastic micromechanical response of two-phase materials using Fast Fourier Transforms. *Int. J. Plasticity* 27, 707–727.
- Lefebvre, G., Sinclair, C., Lebensohn, R., Mithieux, J.D., 2012. Accounting for local interactions in the prediction of roping of ferritic stainless steel sheets. *Model. Simul. Mater. Sci. Eng.* 20, 024008.
- Malvern, L.E., 1969. *Introduction to the Mechanics of a Continuous Medium*. Prentice-Hall, Inc., Englewood Cliffs, New Jersey, USA.
- Michel, J., Moulinec, H., Suquet, P., 2001. A computational scheme for linear and non-linear composites with arbitrary phase contrast. *Int. J. Numer. Methods Eng.* 52, 139–160.
- Mika, D., Dawson, P., 1999. Polycrystal plasticity modeling of intracrystalline boundary textures. *Acta Mater.* 47, 1355–1369.
- Moulinec, H., Suquet, P., 1994. A fast numerical method for computing the linear and nonlinear properties of composites. *C.R. Acad. Sci. Paris Ser. II* 318, 1417–1423.
- Moulinec, H., Suquet, P., 1998. A numerical method for computing the overall response of nonlinear composites with complex microstructure. *Comput. Methods Appl. Mech.* 157, 69–94.
- Mura, T., 1987. *Micromechanics of Defects in Solids*, second ed. Martinus Nijhoff Publishers, Dordrecht.
- Peirce, D., Asaro, R., Needleman, A., 1982. An analysis of nonuniform and localized deformation in ductile single crystals. *Acta Metall.* 30, 1087–1119.
- Prakash, A., Lebensohn, R., 2009. Simulation of micromechanical behavior of polycrystals: finite elements versus fast Fourier transforms. *Model. Simul. Mater. Sci. Eng.* 17, 064010–64016.
- Rossiter, J., Brahme, A., Inal, K., Mishra, R., 2011. Distribution of stress triaxiality in face-centered cubic polycrystals under equibiaxial loading. *Scripta Mater.* 65, 183–185.
- Roters, F., 2011. *Advanced Material Models for the Crystal Plasticity Finite Element Method – Development of a General CPFEM Framework*. Habilitation Thesis. RWTH Aachen, Aachen.
- Roters, F., Eisenlohr, P., Hantcherli, L., Tjahjanto, D., Bieler, T., Raabe, D., 2010. Overview of constitutive laws, kinematics, homogenization, and multiscale methods in crystal plasticity finite element modeling: theory, experiments, applications. *Acta Mater.* 58, 1152–1211.
- Roters, F., Eisenlohr, P., Kords, C., Tjahjanto, D., Diehl, M., Raabe, D., 2012. DAMASK: the Düsseldorf Advanced Material Simulation Kit for studying crystal plasticity using an FE based or a spectral numerical solver. In: Cazacu, O. (Ed.), *Procedia IUTAM: IUTAM Symposium on Linking Scales in Computation: From Microstructure to Macroscale Properties*, vol. 3. Elsevier, Amsterdam, pp. 3–10.
- Suquet, P., Moulinec, H., Castelnau, O., Montagnat, M., Lahellec, N., Grennerat, F., Duval, P., Brenner, R., 2012. Multi-scale modeling of the mechanical behavior of polycrystalline ice under transient creep. In: Cazacu, O. (Ed.), *Procedia IUTAM: IUTAM Symposium on Linking Scales in Computation: From Microstructure to Macroscale Properties*, vol. 3. Elsevier, Amsterdam, pp. 64–78.
- Venkataramani, G., Kirane, K., Ghosh, S., 2008. Microstructural parameters affecting creep induced load shedding in Ti-6242 by a size dependent crystal plasticity FE model. *Int. J. Plasticity* 24, 428–454.
- Zienkiewicz, O., 1967. *The Finite Element Method in Structural and Continuum Mechanics*. McGraw-Hill, New York.